A&A 391, 1–12 (2002)
DOI: 10.1051/0004-6361:20020733

Astronomy & Astrophysics

HST STIS observations of four QSO pairs[⋆]

B. Aracil[1], P. Petitjean[1,2], A. Smette[3,4], J. Surdej[4,5], J. P. Mücket[6], and S. Cristiani[7,8]

[1] Institut d'Astrophysique de Paris – CNRS, 98bis boulevard Arago, 75014 Paris, France
[2] LERMA, Observatoire de Paris, 61 avenue de l'Observatoire, 75014 Paris, France
[3] Chercheur qualifié et Collaborateur Scientifique, Fonds National de la Recherche Scientifique, Belgium
[4] Institut d'Astrophysique et de Géophysique, Université de Liège, Avenue de Cointe 5, 4000 Liège, Belgium
[5] Directeur scientifique, Fonds National de la Recherche Scientifique, Belgium
[6] Astrophysikalisches Institut Potsdam, An der Sternwarte, Potsdam, Germany
[7] Space Telescope European Coordinating Facility, Karl-Schwarzschild Str. 2, 85748 Garching, Germany
[8] Osservatorio Astronomico di Trieste, via G.B. Tiepolo 11, 34131 Trieste, Italy

Received 26 November 2001 / Accepted 15 May 2002

Abstract. We present *HST* STIS observations of four quasar pairs with redshifts $0.84 < z_{\rm em} < 1.56$ and angular separation 2–3 arcmin corresponding to ∼1–1.5 h_{50}^{-1} Mpc transverse proper distance at $z \sim 0.9$. We study the distribution of velocity differences between nearest neighbor H I Lyman-α absorption lines detected in the spectra of adjacent QSOs in order to search for the possible correlation caused by the extent or the clustering properties of the structures traced by the absorption lines over such a scale. The significance of the correlation signal is determined by comparison with Monte-Carlo simulations of spectra with randomly distributed absorption lines. We find an excess of lines with a velocity separation smaller than $\Delta V = 500$ km s^{-1} significant at the 99.97% level. This clearly shows that the Lyman-α forest is correlated on scales larger than 1 h_{50}^{-1} Mpc at $z \sim 1$. However, out of the 20 detected coincidences within this velocity bin, 12 have $\Delta V > 200$ km s^{-1}. This probably reflects the fact that the scale probed by our observations is not related to the real size of individual absorbers but rather to large scale correlation. Statistics are too small to conclude about any difference between pairs separated by either 2 or 3 arcmin. A damped Lyman-α system is detected at $z_{\rm abs} = 1.2412$ toward LBQS 0019−0145A with log N(H I) ∼ 20.5. From the absence of Zn II absorption, we derive a metallicity relative to solar [Zn/H] < −1.75.

Key words. quasars: absorption lines – galaxies: ISM – galaxies: halo

1. Introduction

Recent N-body numerical simulations reproduce successfully the global characteristics of the neutral hydrogen absorptions observed in quasar spectra, the so-called Lyman-α forest (Cen et al. 1994; Petitjean et al. 1995; Hernquist et al. 1996; Zhang et al. 1995; Mücket et al. 1996; Miralda-Escudé et al. 1996; Bond & Wadsley 1998). The absorptions arise from density inhomogeneities in a smooth all-pervading intergalactic medium. Simulations show that the intergalatic gas traces the potential wells of the dark matter well at high redshift. It is therefore possible to constrain the characteristics of the dark-matter density field from observation of the Lyman-α forest along a single line of sight (Croft et al. 2000). The addition of transverse information from observation of QSO pairs or more generally groups of quasars at small projected separation in the sky will probably revolutionize this field in the next few years (Petitjean 1997). Indeed, inversion methods that have been recently implemented show that it is possible to recover the 3D topology of the dark-matter field using a dense network of lines of sight (Nusser & Haehnelt 1998; Pichon et al. 2001; Rollinde et al. 2001).

After the early discovery of common absorptions in pairs of quasars (Shaver et al. 1982; Shaver & Robertson 1983; Weyman & Foltz 1983; Foltz et al. 1984), it was shown that the gaseous complexes giving rise to the absorptions should have large dimensions. In particular, studies of gravitationally lensed quasars (Smette et al. 1992; Smette et al. 1995) yielded a lower limit of 100 h_{50}^{-1} kpc on the diameter of Lyman-α absorbers. Similar results were obtained from pairs of quasars with small separation (Bechtold et al. 1994; Dinshaw et al. 1994; Petitjean et al. 1998; D'Odorico et al. 1998; Monier et al. 1998). Larger separations have been investigated by Crotts & Fang (1998), Dinshaw et al. (1998), Monier et al. (1999)

Send offprint requests to: B. Aracil, e-mail: `aracil@iap.fr`

[⋆] Based on observations with the NASA/ESA *Hubble Space Telescope*, obtained at the Space Telescope Science Institute, which is operated by the Association of Universities for Research in Astronomy, Inc., under NASA contract NAS5-26555. Based on observations carried out at the European Southern Observatory (ESO, programme No. 66.A-0624) with UVES on the 8.2 m VLT-Kuyen telescope operated at Paranal Observatory; Chile.

Table 1. List of observed QSOs.

Object name	$z_{\rm em}$	$\Delta\theta^a$	Δz^b	$< S >^c$
LBQS0019-0145A	1.59			
LBQS0019-0145B	1.04	3.3	0.70−1.01	1640
Q0035-3518	1.20			
Q0035-3520	1.52	3.4	0.69−1.17	1710
Q0037-3545	1.10			
Q0037-3544	0.84	1.7	0.59−0.82	810
PC1320+4755A	1.56			
PC1320+4755B	1.11	1.9	0.62−1.08	940

[a] Angular separation on the sky in arcmin.

[b] Redshift range over which coincidences were searched for.

[c] Mean proper distance in kpc between lines of sight in the redshift range ($q_0 = 0.5, \Lambda = 0, H_0 = 50$ km s^{-1} Mpc^{-1}).

and Williger et al. (2000). All studies conclude that absorptions are correlated on scales larger than 500 h_{50}^{-1} kpc.

Unlike the case of QSO pairs with small angular separations where the correlation can be explained by the fact that the lines of sight intercept the same absorber, the correlation for larger separations is certainly due to the clustering properties of distinct clouds. When observing triplets of quasars separated by 1 to 2 arcmin on the sky, corresponding to ∼0.5 to 1 Mpc proper distance scales, both Crotts & Fang (1998) and Young et al. (2001) find statistically significant triple coincidences that they interpret as the presence of sheetlike structures along which inhomogeneous absorbers cluster.

The number of such experiments is small however and it is important to increase the statistics. Here we present *HST* observations of four pairs of quasars. The ∼2 and ∼3 arcmin angular separations between the two quasars of each pair probes scales between 1.0 and 1.5 h_{50}^{-1} Mpc proper distance at $z \sim 1$. This is where the transition between individual halos and filamentary or sheet-like large scale structures is expected (Mücket et al. 1996; Charlton 1997).

We describe the observations in Sect. 2 and comment on individual metal line systems in Sect. 3. Correlations between metal line and Lyman-α systems are respectively discussed in Sects. 4 and 5. Conclusions are drawn in Sect. 6.

2. Observations

Observations were carried out on the *Hubble Space Telescope* using the Space Telescope Imaging Spectrograph (STIS) with the G230L grating and the Near-UV-MAMA detector. This configuration yields a mean spectral resolution of $R = 700$ ($FWHM = 3.4$ Å at $\lambda = 2374$ Å) and a wavelength coverage from 1570 Å to 3180 Å. The observations were reduced at the Goddard Space Flight Center with the STIS Investigation Definition Team (IDT) version of CALSTIS (Lindler 1998). Standard reduction and calibration were used. Special care was taken to determine accurately the background due to the sky and the dark current. The zero point of the wavelength scale for individual exposures was determined requiring the Galatic interstellar absorptions to occur at rest. The correction can always be performed because the Galactic Mgɪɪ doublet is well detected in every single spectrum. When the Feɪɪ lines were also detected we checked that the dispersion in the zero point is smaller than the spectral resolution. The resulting spectra are shown in Fig. 1. The quasar continuum was fitted with Gaussian profiles for emission lines and simple cubic splines in regions between emission lines. The best fit was found by varying the position of the control points of the cubic splines. The resulting continuum was slightly manually adjusted in regions that were poorly fitted as for example near broad emission lines and Lyman limits. The detection of absorption lines in the normalized spectrum was performed by filtering each spectrum to improve the contrast between lines and noise. This has been performed by successively applying a wavelet filter and an "upgraded" median filter to the spectrum.

We used for the wavelet filter B3-spline scaling functions. This filter selects the wavelength scales corresponding to the width of the absorption lines (see panel b of Fig. 2). Pixels from the wavelet filtered spectra are sorted in increasing order keeping trace of the pixel permutations. The distribution of the pixel values is shown in panel c of Fig. 2. A lower limit of the level of noise in each pixel can be estimated (dashed line) and substracted to the real pixel value (panel d in Fig. 2). Pixels are then reordered and the resulting spectrum is shown in panel e of Fig. 2. This filtered spectrum is used to define regions where possible absorption lines are present using a threshold defined so that no line is lost in the next step. We then compute in the original spectrum the equivalent width and the associated noise over each of these regions and select only those with an equivalent width to noise ratio larger than 2. The corresponding regions are then fitted with a Voigt profile fitting program to derive the position of absorption features. This software makes a χ^2 minimisation in each region adding lines until the reduced χ^2 reaches a value lower than or equal to 1.

For each absorption feature, we calculate the equivalent width in windows centered on the minimum of the line and of widths an increasing number of pixels. The signal-to-noise ratio computed from the noise spectrum is plotted as a function of the distance to the central pixel (panel f of Fig. 2). The S/N ratio of the line was taken at the maximum of the curve and the equivalent width was computed by integrating the fitted profile. The lines with S/N ratio greater than 4 are listed with their identification in Tables 2 to 5. In these tables, uncertain positions or identifications are indicated by a colon.

3. Comments on individual metal line systems

In this section we comment on the intervening metal line systems identified in the spectra. To refer to an absorption feature, we use the numbering given in Tables 2 to 5.

3.1. LBQS 0019−0145A $z_{\rm em}$ = 1.59

The *HST* data on this quasar have been complemented with a high resolution ($R \sim 40\,000$) UVES spectrum covering the wavelength ranges 3900−5200 Å and 5450−9300 Å. The exposure time was two hours.

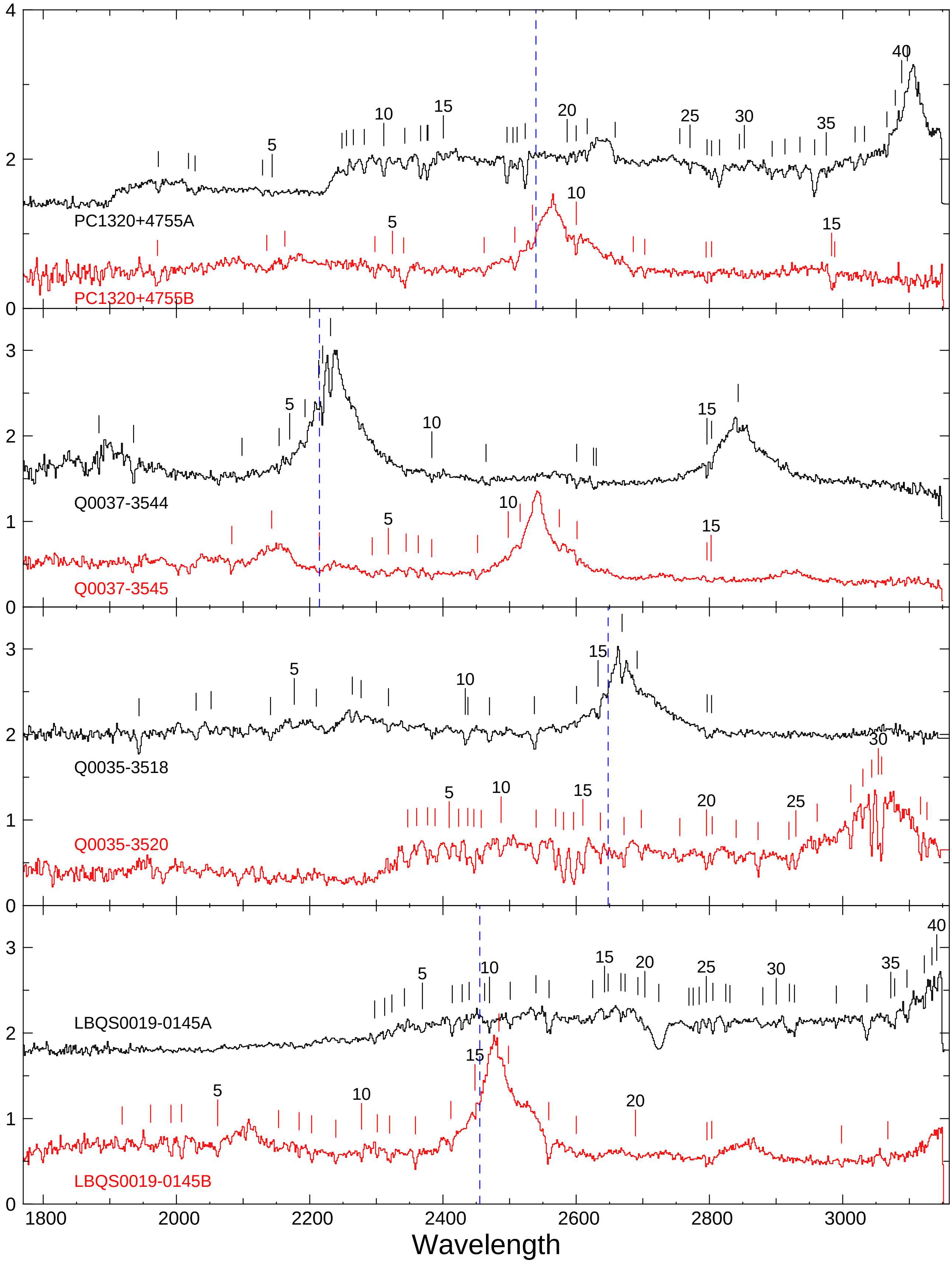

Fig. 1. *HST* STIS spectra of the eight observed quasars. The tick marks indicate significant ($>4\sigma$) absorption features. The vertical dashed lines mark the red limit of the wavelength range for the selection of the Lyman-α lines. This limit is defined by the wavelength at which a line lies at more than 3000 km s^{-1} blueward of the Lyman-α emission line of the lowest redshift quasar in a given pair.

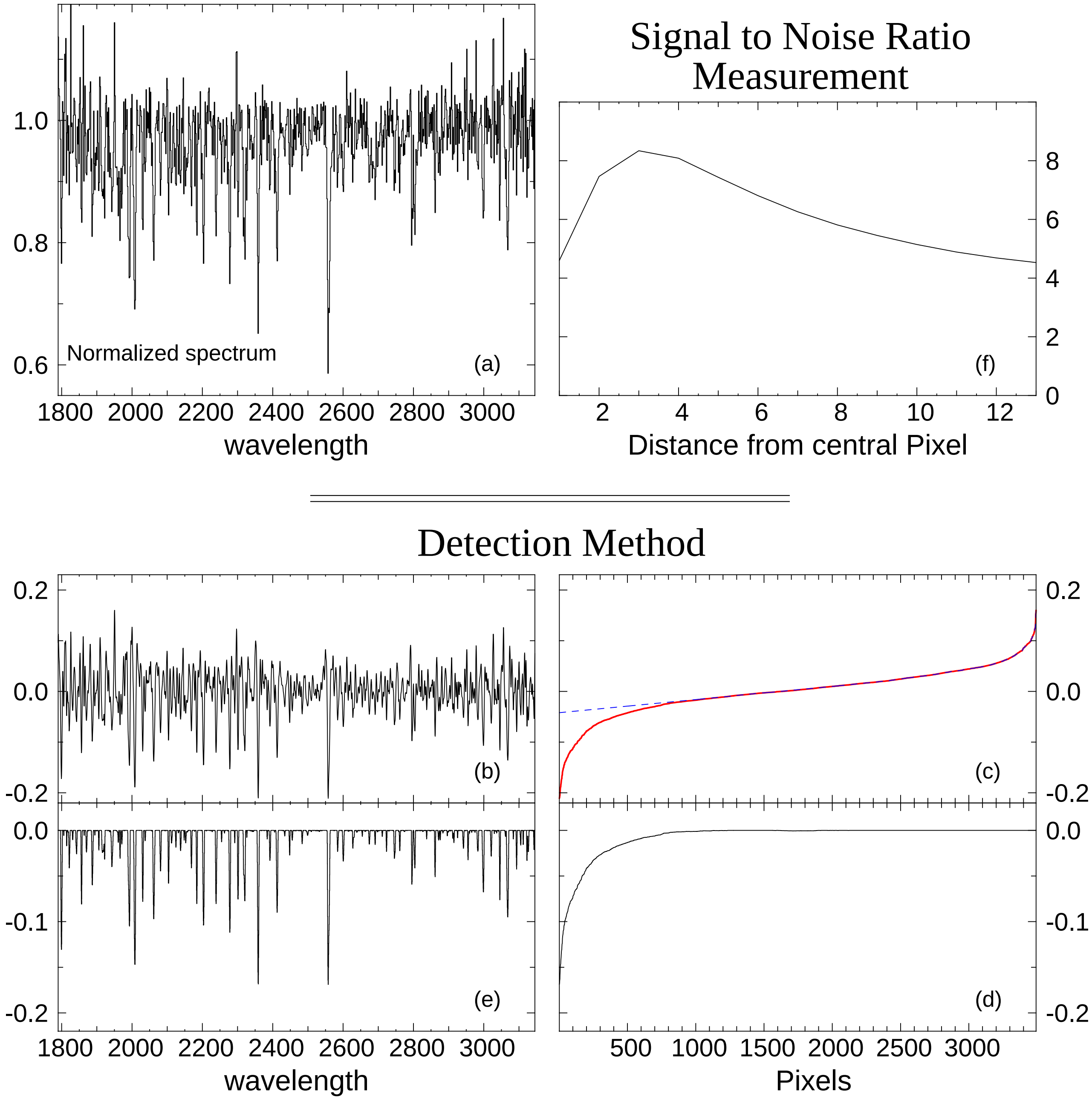

Fig. 2. Illustration of the procedure used to detect absorption lines. Panel **a)** represents the original normalized spectrum which is wavelet filtered to select scales characteristic of the absorption lines. The filtered spectrum is shown in panel **b)**. All pixels in the spectrum are sorted according to their value (panel **c)**). Low values correspond to absorption and high values to spikes; the intermediate values are dominated by noise which is fitted by the dashed line in panel **c)**. This level of noise is subtracted to each pixel to give the new distribution of panel **d)** and pixels are reordered. The resulting spectrum is shown in panel **e)**. This spectrum is used only to select the regions where absorption lines are detected. The equivalent width of each absorption feature is measured in the original spectrum. For each line, the signal to noise ratio is plotted as a function of the distance to the central pixel (panel **f)**). The S/N ratio of the line is taken at the maximum of the curve.

3.1.1. $z_{\rm abs}$ = 0.6514

The strong absorption feature #13 at $\lambda2559.23$ cannot be explained by Lyman-β at $z_{\rm abs} = 1.4976$ alone because the corresponding equivalent width is too large. As there is a strong C IV system at $z_{\rm abs} = 0.65142$ in the spectrum of LBQS 0019−0145B, we tentatively note that the additional absorption could be due to C IV at $z_{\rm abs} = 0.6514$. The corresponding Lyman-α absorption is unfortunately redshifted below the Lyman limit of the $z_{\rm abs} = 1.4976$ system. Mg II$\lambda2803$ at this redshift is not detected in the UVES spectrum down to $w_{\rm obs} = 35$ mÅ.

3.1.2. $z_{\rm abs}$ = 0.6953

Mg II$\lambda2796$ ($w_{\rm e} \sim 0.8$ Å), Fe II$\lambda2382$ ($w_{\rm e} \sim 0.5$ Å), Mg I$\lambda2852$ and Ca II absorptions are detected at this redshift in the UVES spectrum in addition to Al II$\lambda1670$ (line #28) which is

Table 2. Line list for the pair LBQS0019-0145AB.

	LBQS0019-0145A					LBQSQ0019-0145B			
	$\lambda_{\rm obs}$ (Å)	$w_{\rm obs}$ (Å)	Ident.	z		$\lambda_{\rm obs}$ (Å)	$w_{\rm obs}$ (Å)	Ident.	z
					1	1918.43	1.32	Lyα	0.57808
					2	1961.17	1.69	Lyα	0.61324
					3	1991.72	1.70	Lyα	0.63837
								Lyβ	0.94177
					4	2007.78	2.01	Lyα	0.65158
					5	2061.82	1.43	Lyα	0.69604
					6	2153.27	1.08	OI1302	0.65360
					7	2184.12	0.64	Lyα	0.79664
					8	2202.93	1.28	Lyα	0.81211
					9	2239.22	0.84	Lyα	0.84196
					10	2277.89	1.05	Lyα	0.87377
1	2297.48	3.01	Lyβ	1.23987					
					11	2301.37	0.54	SiIV1393	0.65120
2	2312.49	1.64	OVI1031	1.24094					
					12	2319.91	1.56	SiIV1402	0.65381
								Lyα	0.90834
3	2323.35	2.10	OVI1037	1.23912					
			Lyα	0.91117					
4	2342.16	1.69	Lyϵ	1.49750					
			Lyγ	1.40830					
					13	2358.73	1.67	Lyα	0.94027
5	2369.17	2.40	Lyα	0.94886					
					14	2411.93	1.66	Lyα	0.98403
6	2413.95	3.25	Lyα	0.98569					
7	2428.86	1.68	Lyγ	1.49745					
8	2439.36	1.12	Lyα	1.00660					
			CIII977:	1.49672					
					15	2448.06	0.34	Lyα	1.01375
9	2462.56	0.96	Lyα	1.02568					
10	2469.85	1.46	Lyβ	1.40791					
					16	2483.99	0.28	Lyα	1.04331
					17	2498.30	0.45	Lyα	1.05508
11	2500.99	2.28	Lyα	1.05729					
12	2539.55	0.85	Lyα	1.08901					
13	2559.23	4.33	Lyβ	1.49505					
			CIV1548:	0.65171	18	2558.78	3.13	CIV1548	0.65142
			CIV1550:	0.65171				CIV1550	0.65142
					19	2600.10	0.74	FeII2600	0.00000
14	2624.67	1.33	Lyα	1.15903					
15	2642.57	0.63	Lyα	1.17376					
16	2647.93	2.09	Lyα	1.17817					
17	2667.13	1.40	SiII1190	1.24050					
18	2673.36	1.17	SiII1193	1.24033					
					20	2688.92	1.96	…	…
19	2692.54	1.14	ZnI1589	0.69389					
20	2703.05	1.63	SiIII1206	1.24041					
21	2723.96	16.72	Lyα	1.24071					
22	2769.23	2.10	Lyα	1.27795					
23	2775.57	0.87	NV1238	1.24049					
24	2784.59	1.69	Lyα	1.29058					
			NV1242	1.24057					
25	2795.24	1.00	MgII2796	0.00000	21	2796.24	0.80	MgII2796	0.00000
26	2805.20	2.53	MgII2803	0.00000	22	2803.52	0.99	MgII2803	0.00000
			Lyα	1.30876					
27	2824.54	1.98	SiII1260	1.24095					
28	2830.70	0.97	AlII1670	0.69423					
29	2880.13	2.86	Lyα	1.36917					
30	2900.20	0.89	Lyα	1.38568					
31	2920.04	4.75	Lyα	1.40200					
			SiII1304	1.23866					
32	2927.71	1.73	Lyα	1.40831					
33	2990.40	0.84	CII1334	1.24079					
					23	2998.24	0.87	…	…
34	3036.26	5.27	Lyα	1.49760					
					24	3067.77	1.25	…	…
35	3072.23	2.50	Lyα	1.52719					
36	3078.00	1.67	Lyα	1.53194					
37	3096.51	2.09	Lyα	1.54716					
			MgI1827	0.69399					
38	3122.57	0.95	SiIV1393	1.24040					
39	3133.99	0.51	Lyα	1.57799					
40	3141.15	0.50	SiIV1402	1.23925					

detected in the *HST* spectrum. Unfortunately, the H iλ1215 line is redshifted at λ = 2060 Å, below the Lyman limit of the $z_{\rm abs}$ = 1.4976 system.

The profile of the Mg ii and Fe ii absorptions consists of two main absorption features approximately 100 km s^{-1} apart and separated by a sharp drop in optical depth near the center (see Fig. 3). As described by Bond et al. (2001), and despite the moderate Mg iiλ2796 equivalent width, this profile may indicate that the line of sight intercepts a superwind.

Table 3. Line list for the pair LBQS0035-3518 & Q0035-3520.

	Q0035-3518					Q0035-3520			
	$\lambda_{\rm obs}$ (Å)	$w_{\rm obs}$ (Å)	Ident.	z		$\lambda_{\rm obs}$ (Å)	$w_{\rm obs}$ (Å)	Ident.	z
1	1943.74	3.68	Lyα	0.59890					
2	2029.54	2.48	Lyγ	1.08685					
			Lyα	0.66948					
3	2051.99	1.50	Lyβ	1.00053					
4	2141.17	1.25	Lyβ	1.08748					
5	2176.80	1.52	Lyα	0.79062					
6	2209.96	1.11	Lyα	0.81790					
7	2264.01	1.12	OVI1031	1.19396					
8	2277.18	0.78	OVI1037	1.19463					
9	2318.21	1.15	Lyα	0.90694					
					1	2347.06	4.36	Lyα	0.93067
					2	2360.51	0.73	Lyϵ	1.51706
					3	2376.91	1.76	Lyδ	1.50269
					4	2388.14	3.07	Lyδ	1.51451
					5	2409.35	1.24	Lyγ	1.47739
					6	2423.45	1.73	Lyβ	1.36268
								Lyγ	1.49189
10	2433.50	1.38	Lyα	1.00178					
					7	2437.38	2.45	CIII977:	1.49469
								Lyα	1.00497
								Lyγ	1.50621
11	2437.54	1.07	Lyα	1.00510					
					8	2446.42	2.74	CIII977	1.50395
								Lyγ	1.51550
					9	2457.48	2.36	CIII977	1.51527
12	2469.86	1.78	Lyα	1.03169					
					10	2487.20	2.07	Lyα	1.04595
								NIII989	1.51286
13	2537.18	3.74	Lyα	1.08706					
					11	2539.86	2.65	Lyα	1.08927
								Lyβ	1.47617
					12	2569.17	2.20	Lyβ	1.50474
								OVI1037	1.47603
					13	2580.98	5.12	Lyβ	1.51626
								OVI1031	1.50113
					14	2596.06	5.79	OVI1031	1.51574
								OVI1037	1.50195
14	2600.59	0.60	FeII2600	0.00000					
					15	2610.02	3.60	OVI1037	1.51540
15	2632.74	1.56	Lyα	1.16567					
			SiII1260	1.08878					
					16	2636.31	1.15	Lyα	1.16861
16	2668.88	1.85	Lyα	1.19540					
					17	2671.75	1.22	Lyα	1.19776
17	2691.51	0.55	…	…					
					18	2697.75	1.45	Lyα	1.21915
					19	2755.55	1.99	Lyα	1.26669
18	2796.55	1.40	MgII2796	0.00000	20	2795.51	1.82	MgII2796	0.00000
19	2803.19	0.98	MgII2803	0.00000	21	2804.13	1.17	MgII2803	0.00000
					22	2840.11	0.96	Lyα	1.33625
					23	2872.85	2.02	Lyα	1.36318
					24	2919.28	1.23	Lyα	1.40138
					25	2929.73	2.00	Lyα	1.40997
					26	2961.67	0.99	Lyα	1.43625
					27	3012.16	1.78	Lyα	1.47778
					28	3030.27	0.99	Lyα	1.49267
								SiIII1206	1.51162
					29	3043.58	2.49	Lyα	1.50362
					30	3053.48	2.07	Lyα	1.51177
					31	3058.46	3.04	Lyα	1.51586
					32	3116.85	1.91	NV1238	1.51598
					33	3126.49	1.39	NV1242	1.51567

3.1.3. $z_{\rm abs}$ = 1.2412

Strong H iλ1215 (line #21), H iλ1025, Si ii, Si iiiλ1206, Si iv, N v and C iiλ1334 absorptions associated with this system are detected in the *HST* spectrum. Additional Mg ii, Mg iλ2852, Fe ii and Al iiiλ1854, 1862 absorptions are seen in the UVES spectrum (see Fig. 3). Despite the low resolution of the *HST* spectrum, damped wings are clearly seen in the case of the Lyman-α line. The simultaneous fit of the Lyman-α, and Lyman-β absorptions gives log N(H i)~20.5 (see Fig. 4). The observed Fe ii and Mg ii lines are heavily saturated so that only a lower limit on the column densities can be derived, log N(Fe ii & Mg ii) > 15. Zn ii is not detected with log N(Zn ii) < 11.4 implying that metallicity relative to solar, [Zn/H] < −1.75, is one of the smallest observed at low redshift (see e.g. Ledoux et al. 2002). Note that the large column density found for Mg ii

Table 4. Line list for the pair Q0037-3544 & Q0037-3545.

	Q0037-3544					Q0037-3545			
	$\lambda_{\rm obs}$ (Å)	$w_{\rm obs}$ (Å)	Ident.	z		$\lambda_{\rm obs}$ (Å)	$w_{\rm obs}$ (Å)	Ident.	z
1	1883.72	1.09	Lyβ	0.83648					
2	1935.63	2.47	Lyα	0.59223					
					1	2083.05	1.53	Lyα	0.71350
3	2098.4:	1.83							
					2	2142.95	0.76	Lyα	0.76277
4	2154.10	0.83	Lyα	0.77194					
5	2169.85	0.65	Lyα	0.78490					
6	2193.01	1.07	Lyα	0.80395					
7	2213.46	0.49	SiIII1206	0.83461					
					3	2214.50	1.38	Lyα	0.82163
8	2219.40	1.41	SiIV1393	0.59239					
9	2231.31	1.47	Lyα	0.83546					
			SiIV1402	0.59065					
					4	2293.83	1.10	Lyα	0.88689
					5	2318.05	1.25	Lyα	0.90681
					6	2344.75	1.06	FeII2344	0.00000
					7	2362.94	1.08	Lyα	0.94373
10	2383.35	0.55	FeII2382	0.00000	8	2383.15	0.78	FeII2382	0.00000
					9	2451.91	2.01	Lyα	1.01692
11	2464.69	0.91	CIV1548	0.59198					
			CIV1550	0.59198	10	2497.98	0.54	Lyα	1.05482
					11	2515.90	0.90	Lyα	1.06956
					12	2574.68	0.69	...	...
12	2600.73	1.13	FeII2600	0.00000	13	2601.22	0.68	FeII2600	0.00000
13	2626.04	0.75	CIV1548	0.69620					
14	2630.09	0.44	CIV1550	0.69599					
15	2796.30	1.06	MgII2796	0.00000	14	2796.31	0.53	MgII2796	0.00000
16	2803.14	0.95	MgII2803	0.00000	15	2802.46	1.06	MgII2803	0.00000
17	2843.13	0.54	CIV1548	0.83642					
			CIV1550	0.83642					

Table 5. Line list for the pair PC1320+4755AB.

	PC1320+4755A					PC1320+4755B			
	$\lambda_{\rm obs}$ (Å)	$w_{\rm obs}$ (Å)	Ident.	z		$\lambda_{\rm obs}$ (Å)	$w_{\rm obs}$ (Å)	Ident.	z
					1	1971.48	3.59	Lyα	0.62172
1	1972.80	3.18	Lyα	0.62281					
			Lyδ	1.07719					
2	2018.05	2.22	Lyα	0.66003					
			Lyγ	1.07504					
3	2027.99	4.29	Lyα	0.66821					
			CIII977	1.07568					
4	2129.14	2.12	Lyβ	1.07575					
					2	2135.50	1.86	Lyα	0.75664
5	2143.58	1.77	Lyα	0.76329					
			OVI1031	1.07726					
					3	2162.70	1.25	Lyα	0.77902
6	2248.40	1.78	Lyα	0.84952					
7	2255.24	1.73	Lyα	0.85514					
8	2265.48	1.52	Lyζ	1.43404					
9	2281.95	1.98	Lyϵ	1.43329					
					4	2297.90	1.18	Lyα	0.89023
10	2311.25	2.02	Lyδ	1.43355					
					5	2324.25	1.06	SiIII1206	0.92644
					6	2341.04	4.28	Lyα	0.92572
11	2342.76	2.19	FeII2344	0.00000					
			Lyα	0.92713					
12	2366.50	2.74	Lyγ	1.43333					
13	2376.31	1.20	CIII977	1.43219					
			FeII2374	0.00000					
			Lyβ	1.31672					
14	2377.59	3.49	Lyα	0.95579					
15	2400.60	0.73	Lyα	0.97471					
					7	2461.75	1.30	Lyα	1.02502
16	2496.13	3.61	Lyβ	1.43353					
17	2505.12	0.81	SiIII1206	1.07635					
					8	2507.87	1.57	OI1302	0.92592
18	2511.28	1.55	OVI1031	1.43358					
19	2523.50	4.39	Lyα	1.07581					
			OVI1037	1.43202					
					9	2534.39	1.49	Lyα	1.08477
20	2586.44	0.64	FeII2586	0.00000					
21	2599.93	0.40	FeII2600	0.00000	10	2600.13	0.87	FeII2600	0.00000
22	2616.47	1.07	SiII1260	1.07587					
23	2658.55	0.95	Lyα	1.18690					
					11	2685.61	1.84	SiIV1393	0.92689
					12	2702.93	0.89	SiIV1402	0.92685
24	2755.58	1.07	Lyα	1.26672					
25	2770.80	0.99	CII1334	1.07623					
26	2796.37	0.39	MgII2796	0.00000	13	2794.98	1.39	MgII2796	0.00000
27	2803.19	1.15	MgII2803	0.00000	14	2803.16	0.72	MgII2803	0.00000
28	2815.17	3.26	Lyα	1.31574					
29	2844.86	0.76	Lyα	1.34016					
30	2852.45	0.99	Lyα	1.34640					
31	2894.18	0.78	SiIV1393	1.07653					
32	2913.29	1.42	SiIV1402	1.07681					
			Lyα	1.39645					
33	2935.78	2.11	SiIII1206	1.43330					
34	2957.86	5.90	Lyα	1.43311					
35	2975.35	0.59	Lyα	1.44750					
					15	2983.33	2.75	CIV1548	0.92697
					16	2988.07	1.29	CIV1550	0.92683
36	3018.59	1.95	Lyα	1.48307					
37	3032.67	1.00	Lyα	1.49465					
38	3066.43	0.91	SiII1260	1.43286					
39	3078.95	0.88	Lyα	1.53272					
40	3088.62	1.19	Lyα	1.54067					
41	3097.04	1.05	Lyα	1.54760					

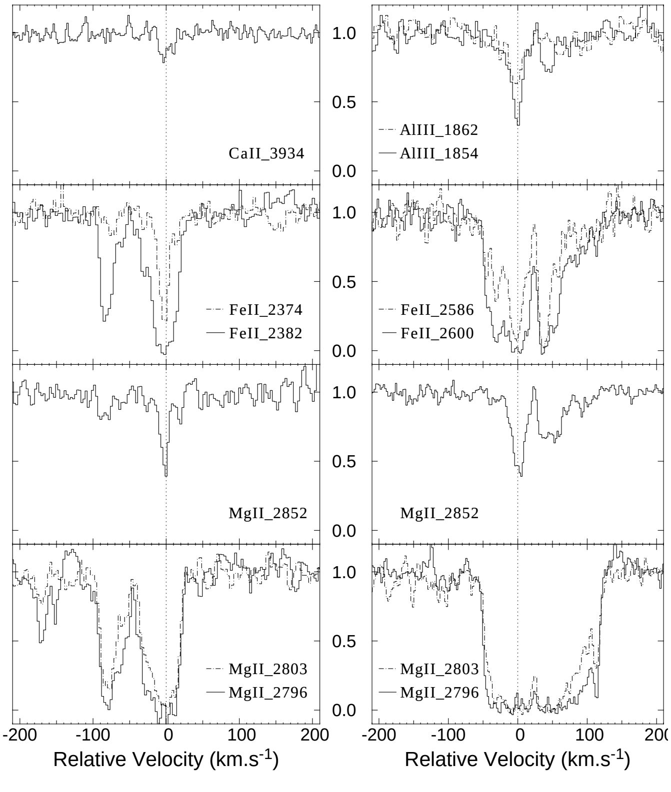

Fig. 3. Metal absorption lines at $z = 0.6953$ (left column) and $z = 1.2412$ (right column, damped Lyman-α system) in the LBQS 0019−0145A UVES spectrum.

implies that the neutral part of the system cannot account for all the MgII we see.

As for the system at $z_{\rm abs} = 0.6953$, the profiles of the absorptions consist of two main components separated by about 50 km s^{-1}. This again may indicate that the line of sight intercepts a superwind.

3.1.4. $z_{\rm abs}$ = 1.3088

The system is unambiguously identified by sharp MgIIλ2796, 2803 absorptions ($w_{\rm r} \sim 0.07$ Å) detected in the UVES spectrum. The Lyman-α absorption is blended with MgIIλ2796 from the interstellar medium.

3.1.5. $z_{\rm abs}$ = 1.4976

This strong system is detected by HIλ1215, 1025, 972, 949, 937 and CIIIλ977 absorptions. It is at the origin of the Lyman limit at $\lambda \sim 2270$ Å and therefore log N(HI) > 18. A possible MgIIλ2796 absorption line is present in the UVES spectrum with $w_{\rm obs} \sim 25$ mÅ.

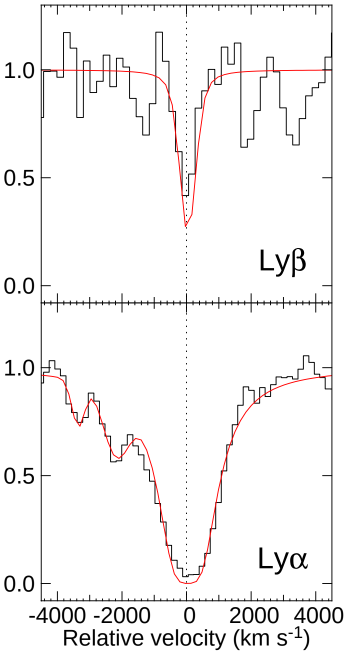

Fig. 4. Lyman-α and Lyman-β absorptions centered at $z_{\rm abs}$ = 1.2412 toward LBQS 0019−0145A. The continuous curve is the best fit to the two Hi absorptions obtained with log N(Hi) ∼ 20.5.

3.2. LBQS 0019–0145B $z_{\rm em}$ = *1.04*

Only one metal line system along this line of sight is detected at $z_{\rm abs}$ = 0.6513 by Hiλ1215, Civλ1548, 1550 and Siivλ1393, 1402 absorptions.

3.3. Q 0035–3518 $z_{\rm em}$ = *1.20*

3.3.1. $z_{\rm abs}$ = 1.088

Strong Hiλ972, 1025, 1215 and Siiiλ1260 absorptions are detected in this system. The latter line is probably blended with another Lyman-α line however. Moreover, an absorption feature detected at the 2.5σ level is observed at the expected position of Ciiλ1334 at λ ∼ 2785 Å.

3.3.2. $z_{\rm abs}$ = 1.1954

This system is at slightly larger redshift than the quasar (∼+1200 km s^{-1}). It shows strong associated Ovi absorption. Nvλ1238 is detected at the 2.5σ level.

3.4. Q 0035–3520 $z_{\rm em}$ = *1.52*

The four metal line systems detected in this quasar are all within 3500 km s^{-1} from the emission redshift of the quasar. As they are approximately at the same redshift, their Lyman-β and Ovi absorptions are blended. The resulting blend corresponds to the four strong features seen at λ ∼ 2600 Å in Fig. 1.

3.4.1. $z_{\rm abs}$ = 1.4927

The Lyman-β line of this system is observed at λ ∼ 2550 Å, but is below the 4σ detection limit. As no other metal line is detected, the Ciiiλ977 identification is tentative and the feature at λ2437.38 could be a blend of Lyman-γ at $z_{\rm abs}$ = 1.50621 and Lyman-α at $z_{\rm abs}$ = 1.00492.

3.4.2. $z_{\rm abs}$ = 1.50362

This system consists of Hiλ949, 972, 1025, 1215, Ovi and Ciiiλ977 absorptions. A feature is also observed at the expected wavelength of the associated Siiiiλ1206 absorption (λ∼3020 Å).

3.4.3. $z_{\rm abs}$ = 1.5118

Hiλ1025, 1215, Ovi, Ciiiλ977 and Siiiiλ1206 are observed at this redshift.

3.4.4. $z_{\rm abs}$ = 1.5158

This system has all the characteristics of an associated system with very strong Nv and Ovi lines. Therefore the Niii and Ciii identifications are tentative.

3.5. Q 0037–3544 $z_{\rm em}$ = *0.84*

3.5.1. $z_{\rm abs}$ = 0.5922

Strong Hiλ1215 and Civ absorptions are detected. Siivλ1393, 1402 are redshifted at λ2219.4 and 2231.31 Å (lines #8 and #9). Given the strengths of the corresponding absorption features, it is most probable that the two Siiv lines are blended with additional Lyman-α lines. An absorption feature is detected at the expected position of Siiiiλ1206 (λ ∼ 1920 Å) but is below the 4σ threshold.

3.5.2. $z_{\rm abs}$ = 0.6961

This system consists of a Civ doublet detected outside the Lyman-α forest. The Lyman-α absorption is observed at wavelength 2062 Å, but is below the 4σ threshold.

3.5.3. $z_{\rm abs}$ = 0.8364

Hiλ1215, Siiiiλ1206 and Civ absorptions are observed at this redshift. Moreover, a feature is observed at the expected position of Siiiλ1260 (λ ∼ 2316 Å).

3.6. Q 0037–3545 $z_{\rm em}$ = *1.10*

We do not identify any metal line system along this line of sight.

Table 6. List of metal lines for the four pairs.

Ident.	$z_{\rm abs}$	$w_{\rm obs}$			Ident.	$z_{\rm abs}$	$w_{\rm obs}$		
		min[a]	max[a]	4σ[b]			min[a]	max[a]	4σ[b]
LBQS0019-0145A ($z_{\rm em}$ = 1.59)					LBQS0019-0145B ($z_{\rm em}$ = 1.04)				
				24.73	Lyman-α	0.65158		2.01	0.70
C ivλ1548:	0.65171	1.54	1.67	0.54	C ivλ1548	0.65158		2.08	0.40
Al iiλ1670	0.69423		0.97	0.69					0.53
Q0035-3518 ($z_{\rm em}$ = 1.20)					Q0035-3520 ($z_{\rm em}$ = 1.52)				
Lyman-α	1.08706		3.74	0.54					0.58
Si iiλ1260	1.08706	0.00	1.56	0.42					0.61
Lyman-α	1.19540		1.85	0.30					0.65
O viλ1031	1.19540		1.12	0.53					1.33
Q0037-3544 ($z_{\rm em}$ = 0.84)					Q0037-3545 ($z_{\rm em}$ = 1.10)				
Lyman-α	0.59223		2.47	0.79					0.96
C ivλ1548	0.59223		0.61	0.56					0.55
C ivλ1548	0.83642		0.36	0.37					0.72
PC1320+4755A ($z_{\rm em}$ = 1.56)					PC1320+4755B ($z_{\rm em}$ = 1.11)				
				0.52	Lyman-α	0.92572		4.28	0.78
				0.79	C ivλ1548	0.92572		2.75	1.05
Lyman-α	1.07581	2.91	3.28	0.41					0.65
Si iiλ1260	1.07581		1.07	0.44					0.58
Si ivλ1393	1.07581		0.78	0.68					1.05

[a] Minimum an maximum equivalent widths taking into account blending.

[b] Four sigma detection limit.

3.7. PC 1320+4755A $z_{\rm em}$ = 1.56

3.7.1. $z_{\rm abs}$ = 1.0762

Strong H iλ949, 972, 1025, 1215, C iiiλ977, Si iv, Si iiλ1260 and C iiλ1334 absorptions are detected at this redshift. Additional features are observed at the expected wavelengths of the associated N iii989 ($\lambda \sim 2055$ Å) and Si iiλ1190, 1993 ($\lambda \sim 2470$ & 2480 Å). This system is at the origin of the Lyman limit seen at ~1890 Å and therefore log N(H i) > 18.

3.7.2. $z_{\rm abs}$ = 1.4329

Strong H i (from Lyman-α to Lyman-ζ), O vi, Si iiiλ1206 and Si iiλ1260 absorptions are observed. From the partial Lyman limit seen at ~2210 Å, we derive log N(H i) ~ 17.3.

3.8. PC 1320+4755B $z_{\rm em}$ = 1.11

Only one metal line system is detected along this line of sight at $z_{\rm abs}$ = 0.9270. It consists of H iλ1215, Si iiiλ1206, Si iv and C iv absorptions. A feature is observed at the position of the associated Si iiλ1260 ($\lambda \sim 2430$ Å).

4. Correlation of metal line systems

We summarize in Table 6 the metal line systems seen along one line of sight for which the corresponding absorption along the adjacent line of sight could be observed. In case of blending, $w_{\rm obs,min}$ and $w_{\rm obs,max}$ are the minimum and maximum equivalent width of the transition. These values are computed using consistency arguments relating the equivalent widths of lines observed in the same system (see examples in Sect. 5.1). The 4σ detection limits are also indicated.

There are only 6 metal line systems which have all $w_{\rm r}$(Lyman-α) > 1 Å. Apart from the C iv system at $z_{\rm abs}$ = 0.65 toward LBQS 0019−0145B which may have a coincident absorption in LBQS 0019−0145A (see Sect. 3.1.1), none of the other systems are detected along the adjacent line of sight down to a 4σ limit of $w_{\rm r}$(Lyman-α) < 0.40 Å. As the system at $z_{\rm abs}$ = 1.19 toward Q 0035−3518 could be associated with the quasar, this means that out of 5 intervening metal line systems with $w_{\rm r}$(Lyman-α) > 1 Å, only one is present in the two lines of sight.

Correlation of C iv systems however has been claimed on large scales at high redshift (e.g. Williger et al. 1996). Moreover, of the five $w_{\rm r}$ > 0.4 Å Lyman-α systems seen at the same $z \sim 2$ redshift in the three spectra of KP 76, 77 and 78 (triple hits over 2–3 arcmin separations), two show associated C iv although C iv is seen only in about one $w_{\rm r}$ > 0.4 Å Lyman-α system out of ten (Crotts & Fang 1998). All this may indicate that the transverse clustering of C iv systems is less pronounced at $z \sim 1$ than at $z \sim 2$ (see also D'Odorico et al. 2002).

5. Correlation in the Lyman-α forest

5.1. The Lyman-α line list

From the line lists obtained as described in Sect. 2 and given in Tables 2 to 5, we have extracted for each pair of QSOs, a master line-list of Lyman-α lines based on several criteria: (i) we include all isolated lines when no other identification is found; (ii) the lines must be at more than 3000 km s^{-1} blueward of the two Lyman-α emission lines; (iii) we use physical consistency arguments to infer the presence of Lyman-α lines blended with metal lines (for example C ivλ1548 cannot be weaker than C ivλ1550); only limits on the equivalent width can be inferred this way; (iv) we impose some equivalent width threshold. The Lyman-α line list is summarized in Table 7. The columns correspond to: #1 and #6 line number in the spectrum (see Fig. 1); #2 and #7 Lyman-α redshift; #3:#4 and #8:#9 the range in equivalent widths in case of blending (see below); #5 and #10 the 4σ equivalent width detection limit using the width of the line detected along either line of sight.

In LBQS 0019−0145A, absorption #3 cannot only be O viλ1037 as it has $w_{\rm obs}$ = 2.10 Å whereas $w_{\rm obs}$(OVI1031) = 1.64 Å. The hidden Lyman-α line has 0.28 < $w_{\rm obs}$ < 0.49 Å corresponding to the O vi doublet ratio ranging from 1 to 2.

Absorption #8 coincides in redshift with C iii at $z_{\rm abs}$ = 1.49672. However, we consider this identification unlikely. Indeed, the line is quite strong ($w_{\rm obs}$ = 1.12 Å) even though the UVES and STIS spectra do not show any other metal lines at this redshift except for a very weak Mg iiλ2796 line system and a 2.5σ feature shifted by 1.5 Å from the expected position of Si iiiλ1206. Therefore, we identify this line as Lyman-α at $z_{\rm abs}$ = 1.00660.

In LBQS 0019−0145B, the limits on the equivalent width of the Lyman-α line blended with Si ivλ1402 at $z_{\rm abs}$ = 0.65381 in feature #12 are derived applying the doublet ratio to the Si ivλ1393 equivalent width.

In Q 0035−3518, we estimate the equivalent width of Lyman-γ (line #2) from the associated Lyman-α and Lyman-β absorptions.

In Q 0035−3520, for feature #7, we assume that C iiiλ977 at $z_{\rm abs}$ = 1.49469 contributes very little since the associated

Table 7. List of Lyman-α lines for the four pairs.

	$z_{\rm abs}$	$w_{\rm r}^{\rm min}$ (Å)	$w_{\rm r}^{\rm max}$ (Å)	$w_{\rm r,4\sigma}^{\rm a}$ (Å)		$z_{\rm abs}$	$w_{\rm r}^{\rm min}$ (Å)	$w_{\rm r}^{\rm max}$ (Å)	$w_{\rm r,4\sigma}^{\rm a}$ (Å)
	Q0019-0145A					Q0019-0145B			
				5.64	5	0.69604		0.84	0.53
				1.70	7	0.79664		0.36	0.31
				1.50	8	0.81211		0.71	0.41
				0.94	9	0.84196		0.46	0.35
				0.91	10	0.87377		0.56	0.31
				0.71	12	0.90834	0.55	0.63	0.39
3	0.91117	0.28	0.49	0.63					0.38
				0.51	13	0.94027		0.86	0.30
5	0.94886		1.23	0.59					0.42
				0.49	14	0.98403		0.84	0.34
6	0.98569		1.64	0.40					0.30
8	1.00660		0.56	0.39					0.26
				0.30	15	1.01375		0.17	0.17
	Q0035-3518					Q0035-3520			
1	0.59890		2.30	0.85					1.31
2	0.66948	0.83	1.21	0.76					1.29
5	0.79062		0.85	0.54					1.11
6	0.81789		0.61	0.53					1.01
9	0.90694		0.60	0.38					0.56
				0.57	1	0.93067		2.26	0.57
10	1.00178		0.69	0.30					0.33
				0.42	7	1.00497	0.42	0.82	0.41
11	1.00510		0.53	0.34					0.33
12	1.03169		0.88	0.36					0.39
				0.44	10	1.04595	0.00	1.01	0.41
13	1.08706		1.79	0.36					0.41
				0.38	11	1.08927	0.64	1.13	0.40
15	1.16567	0.00	0.72	0.26					0.38
				0.21	16	1.16861		0.53	0.30
	Q0037-3544					Q0037-3545			
2	0.59223		1.55	0.67					0.84
				0.56	1	0.71350		0.89	0.47
3	0.72613		1.06	0.75					0.69
				0.50	2	0.76277		0.43	0.38
4	0.77194		0.47	0.37					0.32
5	0.78490		0.36	0.34					0.35
6	0.80395		0.59	0.33					0.49
				0.31	3	0.82163		0.76	0.51
	PC1320+4755A					PC1320+4755B			
				1.35	1	0.62172		2.21	1.43
1	0.62281	0.94	1.72	1.14					1.22
2	0.66003	0.27	0.89	1.07					1.08
3	0.66821	1.67	1.67	1.31					1.18
				1.65	2	0.75664		1.06	1.09
5	0.76329	0.29	0.51	0.99					0.65
				1.14	3	0.77902		0.70	0.70
6	0.84951		0.96	0.47					0.72
7	0.85514		0.93	0.34					0.58
				0.32	4	0.89023		0.62	0.46
				0.48	6	0.92572		2.22	0.72
11	0.92713	0.97	1.04	0.40					0.61
14	0.95579		1.78	0.43					0.80
15	0.97471		0.37	0.29					0.54
				0.36	7	1.02501		0.64	0.51
19	1.07581	1.40	1.58	0.22					0.41
				0.33	9	1.08477		0.71	0.38

[a] Calculated using the width of the line detected along either line of sight.

Lyman-α absorption is weak and no other metal line is detected; limits on the equivalent width of the Lyman-α line at $z_{\rm abs} = 1.00497$ come from limits on Lyman-γ at $z_{\rm abs} = 1.50621$ derived from the Lyman-α absorption. Similarly, we have constrained the equivalent width of Lyman-β at $z_{\rm abs} = 1.47617$ in the absorption feature #11 from the associated Lyman-α line.

In PC 1320+4755A, the limits on the equivalent width of Lyman-δ (feature #1) and Lyman-γ (feature #2) at $z_{\rm abs} = 1.07575$ come from their associated Lyman-β and Lyman-α absorptions. For feature #3 we assumed for the equivalent width of Ciiiλ977 a conservative limit of 1.5 Å from the associated Ciiλ1334 line. Finally, lower and upper limits on the equivalent width of Oviλ1031 at $z_{\rm abs} = 1.07726$ (feature #5) and Feiiλ2344 at $z_{\rm abs} = 0$ (feature #11) come from Oviλ1037 which has an equivalent width $w_{\rm obs} \sim 0.8$ Å, below the 4σ detection limit, and Feiiλ2600 respectively.

Note that the number of metal lines which could be misidentified as Lyman-α lines is expected to be small. Indeed, they can be neither Mg ii nor Fe ii lines because the strongest potential lines of these species are redshifted beyond the wavelength of the Lyman-α line with the highest redshift in our sample. They cannot be lines too close in wavelength to Lyman-α as our careful procedure would have identified them. The only possibility is that some isolated Al iiλ1670 or C ivλ1548 (with C ivλ1550 not detectable) lines could be present in the wavelength range where we search for coincidences. The number of C iv and Mg ii systems with $w_{\rm r} > 0.3$ Å at $z \sim 0.3$ is 0.87 and 0.75 per unit redshift respectively (Bergeron et al. 1994; Boissé et al. 1992). We consider that half of the Mg ii systems have an associated Al ii line and half of the C iv systems would have only C ivλ1548 detected. Moreover, only less than two-third of these systems have $w_{\rm r} > 0.4$ Å which is the usual 4 σ limit of our spectra. As our survey samples a redshift interval of $\Delta z = 2.96$ (considering six lines of sights, see Table 1), the expected number of misidentified lines is of the order of 1 to 2. This is to be compared to the 46 Lyman-α lines with $w_{\rm r} > 0.4$ Å we detect. Note that the latter number is consistent with the number of lines detected in the *HST* Key-program (Jannuzi et al. 1998).

5.2. Correlation

From the master line list, we selected lines with $w_{\rm r} > 0.3$ Å and applied the Nearest-Neighbor method as described in e.g. Young et al. (2001) to estimate the level of correlation between absorptions detected along adjacent lines of sight. In this method, there is no a priori velocity separation limit in the definition of a coincidence. A couple of lines along two different lines of sight is declared to be a coincidence if each of the lines is the nearest neighbor of the other. Note that the procedure underestimate the clustering signal as it does not take into account the difference of S/N ratio along the two lines of sight.

The distributions of velocity separations ($|\Delta v|$) between the two lines in a coincidence are plotted in Fig. 5 for the pairs with angular separation ~2 arcmin (panel a), 3 arcmin (panel b) and the complete sample (panel c). To improve statistics, we have added to our results, the data of Young et al. (2001) on two additional pairs separated by ~2 arcmin and ~3 arcmin. The results are plotted in Fig. 5 for the pairs with an angular separation ~2 (panel d), 3 arcmin (panel e) and for all the pairs (panel f).

To estimate the excess of correlation with respect to randomly placed absorption lines, we produced 100 000 simulated master line lists drawn from a population of randomly redshifted lines, taking the same number of lines and the same wavelength range as in the observed spectra. Results of applying the same method to the simulated line lists are given as dotted lines in Fig. 5. The error bars in the figure correspond to the rms of the values found in the simulation. As the corresponding distribution is not Gaussian, we indicate in the following the probability that the observed number of coincidences occurs in the simulated population.

We detect 2 and 4 coincidences with $|\Delta v|$ smaller than 500 km s^{-1} in the two pairs separated by ~2 arcmin and

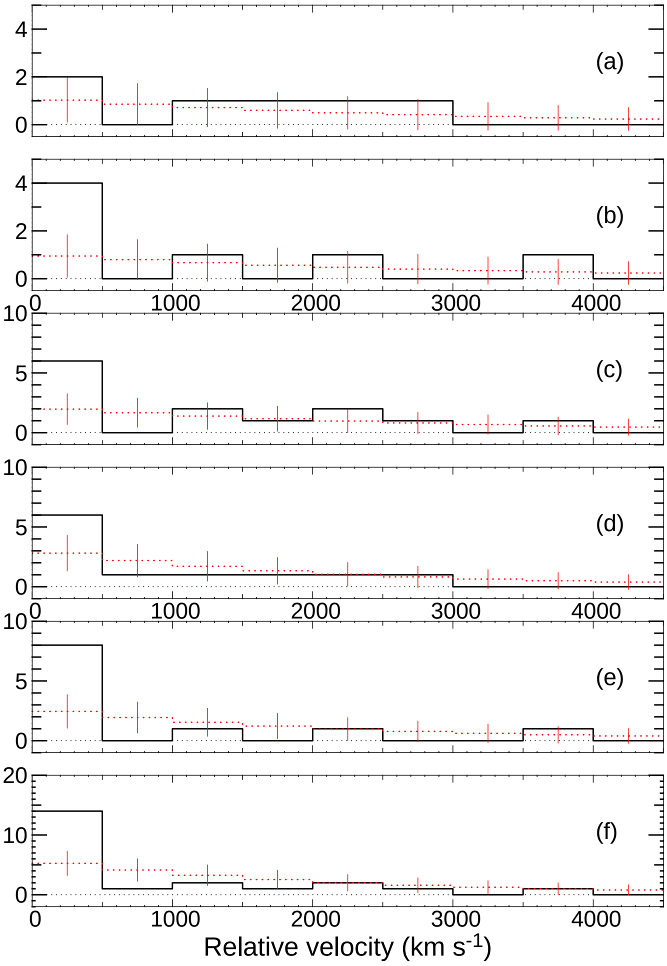

Fig. 5. Number of coincidences versus the velocity separation $|\Delta v|$ between the two lines for rest equivalent width threshold of $w_\mathrm{r} > 0.3$ Å. Panel **a)**: for pairs with separation ~2 arcmin, Q 0037−3544 & Q 0037−3545 and PC 1320+4755A&B; panel **b)**: for pairs with separation ~3 arcmin, LBQS 0019−0145A&B and Q 0035−3518 & Q 0035−3520; panel **c)**: for the four pairs. Panels **d)**, **e)** and **f)** are the same as, respectively, panels **a)**, **b)** and **c)** but after adding data of Young et al. (2001). Dotted lines correspond to the expected number of coincidences from a randomly placed population of lines.

~3 arcmin respectively. The fact that the number of coincidences is smaller in the closest pairs is not statistically significant. When the complete sample is used (panel c of Fig. 5), the excess in the first bin ($|\Delta v| < 500$ km s^{-1}) is significant at the 99.20% level. To increase the statistics, we have added to our sample data from Young et al. (2001). The total number of coincidences with $|\Delta v| < 500$ km s^{-1} and $w_\mathrm{r} > 0.3$ Å is increased to 6, 8 and 14 for the pairs separated by ~2 arcmin, ~3 arcmin and the complete sample. The corresponding excesses relative to simulations of randomly placed lines are significant at the 95.57%, 99.92% and 99.97% levels respectively. The excess is about the same when no threshold is applied to the equivalent width (see Fig. 6). In that case, the number of coincidences in the first bin is 20 and the excess is detected at the 4σ level.

This clearly shows that the Lyman-α forest is correlated on scales larger than 1 h_{50}^{-1} Mpc proper at $z \sim 1$. However, we should note that, in the complete sample, 12 of the 20 coincidences with $|\Delta v|$ smaller than 500 km s^{-1} actually have $|\Delta v|$ greater than 200 km s^{-1}. This is also the case for 8 of the 14 coincidences in the $w_\mathrm{r} > 0.3$ Å sample. These velocity differences are probably related to peculiar velocities of different objects and reveal that the scale we probe is not related to the real size of individual absorbers.

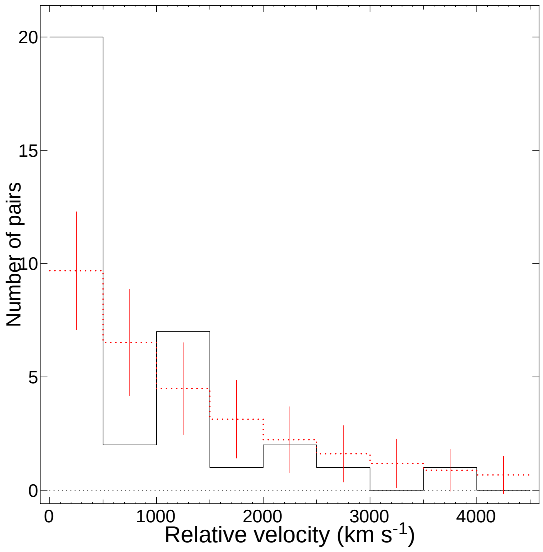

Fig. 6. Number of coincidences versus the velocity separation $|\Delta v|$ between the two lines for the complete sample.

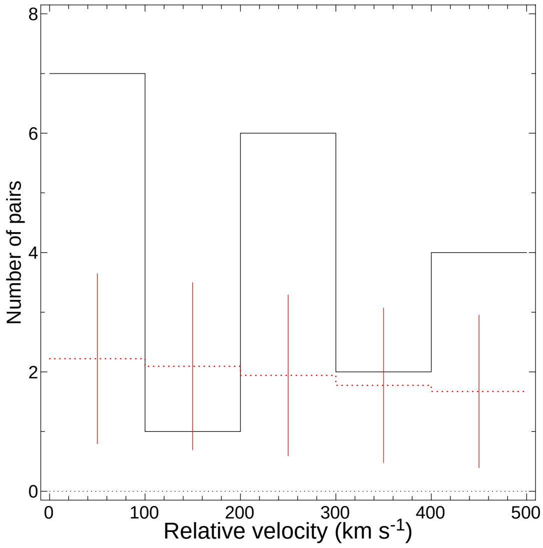

Fig. 7. Velocity distribution of the 20 coincidences with $|\Delta v| < 500$ km s^{-1}. The dotted line indicates the expected number of coincidences from the Monte-Carlo simulations.

In Fig. 8 we plot the equivalent width observed along one line of sight versus the equivalent width observed along the second line of sight for the 20 pairs with velocity differences smaller than 500 km s^{-1}. There is no clear trend in the plot. This is not really surprising as we do not expect the absorption strengths to be correlated at such a separation neither in the case of a common absorber nor in the case of independent objects.

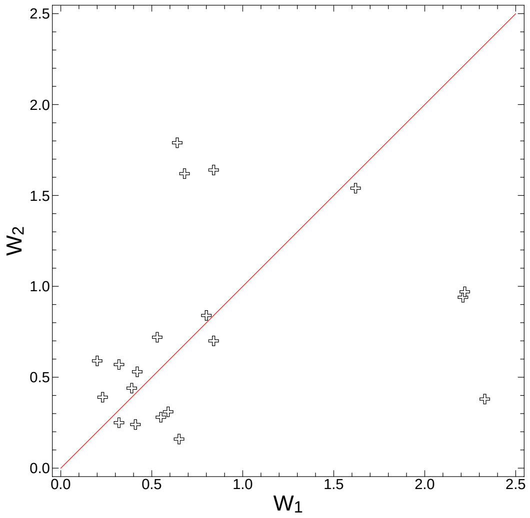

Fig. 8. Equivalent width observed along one line of sight versus the one observed along the second line of sight for the 20 coincidences with velocity difference smaller than 500 km s^{-1}.

6. Conclusion

We have searched for coincidences of Lyman-α absorbers at $z \leq 1$ along the lines of sight toward four pairs of quasars with separations 2−3 arcmin, observed with *HST* STIS. Using the Nearest-Neighbor statistics, we have constructed the distribution of the velocity difference between absorption lines detected along two adjacent lines of sight. We have compared this observed distribution to that derived from Monte-Carlo simulations placing at random the same number of lines in the same wavelength ranges as in the observations. For lines with $w_{\rm r} > 0.3$ Å , we find an excess of coincidences with velocity separations smaller than 500 km s^{-1} significant at the 99.2% level. Combining our data with those in the literature (Young et al. 2001), the excess relative to simulations is significant at the 99.97% level for lines with $w_{\rm r} > 0.3$ Å and at the 99.98% level if no condition on the equivalent width is imposed.

The result is consistent with the findings of similar studies at higher redshift (Crotts & Fang 1998; Williger et al. 2000). There is however an important difference between high and intermediate redshift observations. At high redshift, the excess is seen for velocity separations between two coincident lines smaller than 200 km s^{-1}. At lower redshift, the mean velocity difference is larger (see Fig. 7). This is not a systematic effect related to the low spectral resolution of our data. It could be related to the increase of peculiar velocities with decreasing redshift for comparable spatial scales. This conclusion is strengthened by the fact that the transverse correlation, $\chi \propto \sum_i (1 - F_1(\lambda_i)) \times (1 - F_2(\lambda_i))$ where $F_1(\lambda_i)$ and $F_2(\lambda_i)$ are the two QSO normalized fluxes at wavelength λ_i, at $z \sim 1$ measured on our spectra is very small, $|\chi| < 0.01$, whereas it is of the order of 0.2 at $z \sim 2$ for the same separation (Rollinde et al. in preparation, see also McDonald 2000, 2001; Viel et al. 2002). This can be explained by the fact that large values of χ are due to coincidences with velocity separations smaller than the spectral resolution. In conclusion, evolution from high to low redshift is not seen in the level of correlation but rather in the velocity difference between lines of sight which increases with decreasing redshift. Simulations have shown that absorption lines with a given column density correspond to higher overdensities at low-redshift compared to high redshift and most of the Lyman-α forest at low redshift is to be revealed by very weak lines (Riediger et al. 1998; Theuns et al. 1998; Penton et al. 2000). Therefore, detailed study of the cosmological evolution of the Lyman-α forest will only be possible when the sensitivity of the instruments will be high enough to routinely detect lines with $w_{\rm r} < 0.01$ Å in the UV.

Acknowledgements. We thank Cédric Ledoux for the reduction of the LBQS 0019−0145A UVES spectrum. This work was supported in part by the European RTN program "The Intergalactic Medium" and by a PROCOPE program of bilateral collaboration between France and Germany. BA and PPJ thank AIP for hospitality.

References

Bechtold, J., Crotts, A. P. S., Duncan, R. C., & Fang, Y. 1994, ApJ, 437, L83
Bergeron, J., Petitjean, P., Sargent, W. L. W., et al. 1994, ApJ, 436, 33
Boissé, P., Boulade, O., Kunth, D., Tytler, D., & Vigroux, L. 1992, A&A, 262, 401
Bond, J. R., & Wadsley, J. W. 1998, XIII IAP Workshop, ed. P. Petitjean, & S. Charlot (Éditions Frontières, Paris), 143
Bond, N. A., Churchill, C. W., Charlton, J. C., & Vogt, S. S. 2001, ApJ, 557, 761
Cen, R., Miralda-Escudé, J., Ostriker, J. P., & Rauch, M. 1994, ApJ, 437, L9
Charlton, J. C., Anninos, P., Zhang, Y., & Norman, M. L. 1997, ApJ, 485, 26C
Croft, R. A. C., Weinberg, D. H., Bolte, M., et al. 2000 [`astro-ph/0012324`]
Crotts, A. P. S., & Fang, Y. 1998, ApJ, 502, 16
Dinshaw, N., Impey, C. D., Foltz, C. B., Weymann, R. J., & Chaffee, F. H. 1994, ApJ, 437, L87
Dinshaw, N., Foltz, C. B., Impey, C. D., Weymann, R. J., & Morris, S. L. 1995, Nature, 373, 223
Dinshaw, N., Foltz, C. B., Impey, C. D., & Weymann, R. J. 1998, Nature, 494, 567
D'Odorico, V., Cristiani, S., D'Odorico, S., Fontana, A., Giallongo, E., & Shaver, P. 1998, A&A, 339, 678
D'Odorico, V., Petitjean, P., & Cristiani, S. 2002 [`astro-ph/0205299`]
Foltz, C. B., Weymann, R. J., Röser, H. J., & Chaffee, F. H. 1984, ApJ, 440, 458
Hernquist, L., Katz, N., Weinberg, D. H., & Miralda-Escudé, J. 1996, ApJ, 457, L51
Jannuzi, B. T., Bahcall, J. N., Bergeron, J., et al. 1998, ApJS, 118, 1
Ledoux, C., Bergeron, J., & Petitjean, P. 2002, A&A, 385, 802
Lindler, D. J. 1998, CALSTIS Reference Guide (Version 5.1), `http://hires.gsfc.nasa.gov/stis/software/software.html`
McDonald, P. 2000, AAS, 197, 6602M
McDonald, P. 2001 [`astro-ph/0108064`]
Miralda-Escudé, J., Cen, R., Ostriker, J. P., & Rauch, M. 1996, ApJ, 471, 582
Monier, E. M., Turnshek, D. A., & Lupie, O. L. 1998, ApJ, 496, 177
Monier, E. M., Turnshek, D. A., & Hazard, C. 1999, ApJ, 522, 627
Mücket, J. P., Petitjean, P., Kates, R., & Riediger, R. 1996, A&A, 308, 17

Penton, S. V., Shull, J. M., & Stocke, J. T. 2000, ApJ, 544, 150
Petitjean, P. 1997, in ESO Workshop, The Early Universe with the *VLT*, ed. J. Bergeron, 266
Petitjean, P., Mücket, J. P., & Kates, R. E. 1995, A&A, 295, L9
Petitjean, P., Surdej, J., Smette, A., et al. M. 1998, A&A, 334, L45
Rollinde, E., Petitjean, P., & Pichon, C. 2001, A&A, 376, 28
Riediger, R., Petitjean, P., & Mücket, J. P. 1998, A&A, 329, 30
Sargent, W. L. W., Young, P. J., & Schneider, D. P. 1982, ApJ, 256, 374
Shaver, P. A., Boksenberg, A., & Robertson, J. G. 1982, ApJ, 261, L7
Shaver, P. A., & Robertson, J. G. 1983, ApJ, 268, L57
Smette, A., Robertson, J. G., Shaver, P. A., et al. 1995, A&AS, 113, 199
Smette, A., Surdej, J., Shaver, P. A., et al. 1992, ApJ, 389, 39S
Theuns, T., Leonard, A., & Efstathiou, G. 1998, MNRAS, 297, L49
Viel, M., Matarrese, S., Mo, H. J., Haehnelt, M. G., & Theuns, T. 2002, MNRAS, 329, 848
Weymann, R. J., & Foltz, C. B. 1983, ApJ, 272, L1
Williger, G. M., Hazard, C., Baldwin, J. A., & McMahon, R. G. 1996, ApJS, 104, 145
Williger, G. M., Smette, A., Hazard, C., Baldwin, J. A., & McMahon, R. G. 2000, ApJ, 532, 77
Young, P. A., Impey, C. D., & Foltz, C. B. 2001, ApJ, 549, 76
Zhang, Y., Anninos, P., & Norman, M. L. 1995, ApJ, 453, L57